Article

# Single-defect phonons imaged by electron microscopy

https://doi.org/10.1038/s41586-020-03049-y

Received: 27 October 2019

Accepted: 7 October 2020

Published online: 6 January 2021

Check for updates

Xingxu Yan[1,2], Chengyan Liu[3,4], Chaitanya A. Gadre[3], Lei Gu[3], Toshihiro Aoki[2], Tracy C. Lovejoy[5], Niklas Dellby[5], Ondrej L. Krivanek[5], Darrell G. Schlom[6,7,8], Ruqian Wu[3]✉ & Xiaoqing Pan[1,2,3]✉

Crystal defects affect the thermal and heat-transport properties of materials by scattering phonons and modifying phonon spectra[1–8]. To appreciate how imperfections in solids influence thermal conductivity and diffusivity, it is thus essential to understand phonon–defect interactions. Sophisticated theories are available to explore such interactions, but experimental validation is limited because most phonon-detecting spectroscopic methods do not reach the high spatial resolution needed to resolve local vibrational spectra near individual defects. Here we demonstrate that space- and angle-resolved vibrational spectroscopy in a transmission electron microscope makes it possible to map the vibrational spectra of individual crystal defects. We detect a red shift of several millielectronvolts in the energy of acoustic vibration modes near a single stacking fault in cubic silicon carbide, together with substantial changes in their intensity, and find that these changes are confined to within a few nanometres of the stacking fault. These observations illustrate that the capabilities of a state-of-the-art transmission electron microscope open the door to the direct mapping of phonon propagation around defects, which is expected to provide useful guidance for engineering the thermal properties of materials.

Imperfections such as point defects, dislocations, stacking faults and grain boundaries are often present in crystalline materials and affect their thermal properties, such as thermal conductivity and thermoelectric performance[1]. They play an even more decisive role when the material's dimension is reduced to the nanoscale[2]. Different modelling tools have been developed to understand the interaction between heat and imperfections in solids and to explain the changes of thermal conductivity and diffusivity, which are experimentally obtained using techniques such as time-domain thermoreflectance, the 3ω method and transient grating spectroscopy[3,4,9,10]. In existing thermal transport theories, thermal conductivities of defect-free crystals are computed by solving the Boltzmann transport equation[5]. The effect of defects on thermal transport is typically treated by perturbation theory, which takes into account the mass difference and the change of interatomic force constants[1,5]. State-of-the-art ab initio computations have recently been applied, along with the real-space Green's function approach, to studies of thermal conductivities of materials with defects[4,6,11–13]. Except in the modelling of alloy structures[12,14], much theoretical work dealing with the thermal properties of imperfect structures (especially those with planar defects) has omitted the defect-induced changes in phonon dispersion curves[2,5,8]. The treatment of planar defects—for example, stacking faults—typically only considers the specular reflection[7]. Despite these simplifications, theoretical studies have predicted the existence of local vibrational modes due to point defects or dislocations, and a quasi-phonon model has been proposed to understand the phonon–defect interaction[1,2,8].

A more thorough understanding of phonon–defect interaction, especially the effect of defects on thermal transport, becomes possible if experimental data on both local and non-local phonon modes around defects are available. However, it has not been feasible up to now to reach the required spatial resolution (down to the subnanometre scale) together with an angular (momentum) resolution that allows individual acoustic phonon branches to be identified in reciprocal space. Optical methods such as Raman and infrared spectroscopies can provide hints of local phonon variation, but they are incapable of distinguishing individual defects, because their spatial resolution is limited by the wavelength of the incident light[15–19]. Similarly, inelastic X-ray scattering and inelastic neutron scattering (INS) spectroscopies only detect the averaged signal from larger samples with poor spatial resolution[20,21]. Inelastic electron tunnelling spectroscopy is capable of measuring the vibrational modes of adsorbed molecules in a scanning tunnelling microscope with very high spatial resolution. However, this technique is only sensitive to the first few atomic layers on conductive substrates[22,23]. In summary, probing vibrational modes at local defects deep inside a material has not been realized until now.

Recent advances in monochromated electron energy-loss spectroscopy (EELS) and aberration-corrected scanning transmission electron microscopy (STEM) have substantially improved spectroscopic resolution to <10 meV, and enabled the acquisition of vibrational signals

[1]Department of Materials Science and Engineering, University of California, Irvine, Irvine, CA, USA. [2]Irvine Materials Research Institute, University of California, Irvine, Irvine, CA, USA. [3]Department of Physics and Astronomy, University of California, Irvine, Irvine, CA, USA. [4]Key Laboratory for Special Functional Materials of Ministry of Education, School of Materials Science and Engineering, Henan University, Kaifeng, China. [5]Nion R&D, Kirkland, WA, USA. [6]Department of Materials Science and Engineering, Cornell University, Ithaca, NY, USA. [7]Kavli Institute at Cornell for Nanoscale Science, Ithaca, NY, USA. [8]Leibniz-Institut für Kristallzüchtung, Berlin, Germany. ✉e-mail: wur@uci.edu; xiaoqing.pan@uci.edu

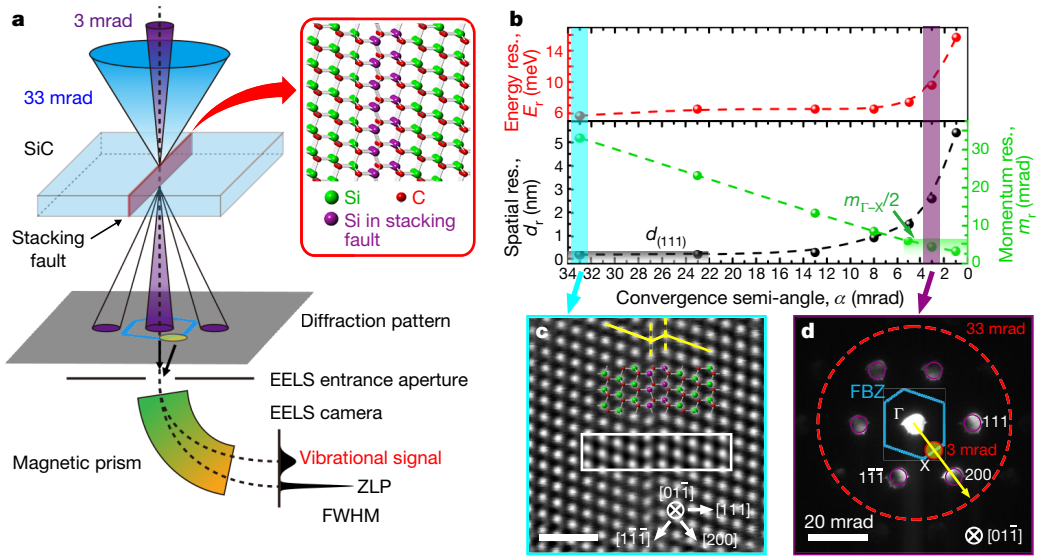


**Fig. 1 | Experimental setup of high-spatial-resolution imaging and optimal-momentum-resolution vibrational spectroscopy of a single stacking fault in 3C-phase SiC. a**, Schematic of the experimental setup. The convergent electron probe with a tunable convergence semi-angle $\alpha$ (defined as the size of the probe-forming aperture and set to 33 mrad or 3 mrad) is formed and raster-scanned across the sample with an edge-on stacking fault. Inset, the atomic structure at the stacking fault. Green and red balls are Si and C atoms respectively, and the purple balls are the Si atoms at the stacking fault, shown to highlight the structural difference. The purple disks in the diffraction plane (shown grey) are transmitted and diffracted electrons, and the yellow disk represents the X point at the edge of first Brillouin zone (FBZ, blue contour). See Methods for further details. **b**, The impact of probe convergence semi-angle ($\alpha$) on the energy ($E_r$), spatial ($d_r$) and momentum ($m_r$) resolution. The dashed lines in both top and bottom panels are guides to the eye. The grey shaded area shows the optimal range for resolving the stacking-fault structure, while the green shaded area is ideal for fully separating the Γ and X points in the FBZ. **c**, Atomic-resolution annular dark-field (ADF) STEM image of a cross-sectional SiC specimen with a single stacking fault projected along the [01$\bar{1}$] direction, with $\alpha = 33$ mrad (4.3 Å$^{-1}$) indicated by the cyan bar in **b**. Scale bar, 1 nm. The atomic structure and a simulated STEM image (white box) are both superimposed on the STEM image. **d**, Diffraction pattern of SiC along the [01$\bar{1}$] direction with $\alpha = 3$ mrad (0.39 Å$^{-1}$) as marked by the purple bar in **b**. The large red dashed circle and the small red circle correspond to convergence semi-angles of 33 mrad and 3 mrad, respectively. 200, 111 and 1$\bar{1}\bar{1}$ diffraction spots are marked by purple circles. Scale bar, 20 mrad.

with high spatial resolution[24–26]. The study of phonon interaction with defects using EELS in TEM requires that multiple phonon branches be resolved and investigated separately because of the complexity of phonon dispersion relations, and this becomes feasible with angle-resolved EELS. Moreover, phonons strongly scattered by localized defects are more readily identifiable by selecting high-angle scattering events of fast electrons with an off-axis EELS entrance aperture.

In this study, we initially explore the local phonon spectral density at high spatial resolution by forming an electron probe with a large convergence angle, and collecting EEL spectra spanning a large angular (momentum exchange) range. However, this results in summing all the phonon dispersion branches together, and it makes direct comparison with spectra acquired by optical methods or INS impracticable[27–29]. We therefore improve the angular (momentum) resolution so as to resolve different phonon modes, which leads to poorer, but still nanometre-level, spatial resolution[30]. The improved momentum resolution also identifies the splitting of longitudinal optical (LO) and transverse optical (TO) phonons without the interference of phonon polaritons in polar crystals[24,26,27,31,32]. Our method enables us to simultaneously achieve sufficient momentum resolution and high spatial resolution, and to exclude polariton signals. It unveils local phonon resonances caused by symmetry breaking at a stacking fault in silicon carbide (SiC).

SiC was selected as a suitable model material because of its wide range of applications in electronic devices and its abundant polytypes with various stacking orders[16,33]. Stacking faults are common imperfections in SiC crystals, arising from local stacking disorder of the {111} planes, and it markedly affects the thermal conductivity[34]. Isolated stacking faults can be easily found in 3C-phase SiC films grown on a Si substrate[35,36], owing to a large lattice mismatch of 24.5% between SiC and Si, as shown in Extended Data Fig. 1. Figure 1a illustrates the experimental setup aiming to acquire local vibrational information at a single defect. The convergence semi-angle ($\alpha$) is critical in controlling the spatial resolution ($d_r$), momentum resolution ($m_r$) and energy resolution ($E_r$) as shown in Fig. 1b. Figure 1c displays a single edge-on stacking fault in 3C-phase SiC projected along the [01$\bar{1}$] zone axis, with convergence semi-angle $\alpha = 33$ mrad forming an electron probe with a size of about 0.14 nm. The resultant annular dark-field (ADF) STEM image is consistent with the defect atomic structure and with the simulated image. The width of the stacking fault is 0.25 nm, matching the (111) inter-planar distance. Since $d_r$ is inversely proportional to $\alpha$ (see more details in Methods)[37], $\alpha$ should be greater than 22 mrad to resolve the stacking fault in real space. In reciprocal space, acoustic phonon modes reach their highest energy (and become easiest to detect) at the edge of the Brillouin zone (BZ). In the diffraction pattern obtained with $\alpha = 3$ mrad (0.39 Å$^{-1}$) in Fig. 1d, the X point is well suited to acquiring an angle-resolved vibrational signal. Because the momentum resolution is improved as $\alpha$ decreases, $\alpha$ should be smaller than 5.5 mrad (0.71 Å$^{-1}$, half the reciprocal distance between Γ and X) to fully separate the Γ and X points (Fig. 1d and Extended Data Fig. 2). Therefore, we developed a combined method to take advantage of both wide and narrow aperture settings for a systematic study of vibrational signals of an isolated crystal defect.

Figure 2a shows background-subtracted vibrational spectra taken from a defect-free region and an edge-on stacking-fault region in SiC, with a convergence semi-angle of 33 mrad. On the basis of the first-principles calculations (Fig. 2b) and published Raman and INS data[38–40], the LO and TO modes are located at respectively 120 meV and 98 meV at the Γ point, while LO, TO and longitudinal and transverse acoustic (LA and TA) modes coexist at respectively 104 meV, 95 meV, 79 meV and 46 meV at the X point. In the experimental vibrational spectra (Fig. 2a), the first two peaks at 108.6 meV and 98.2 meV can be

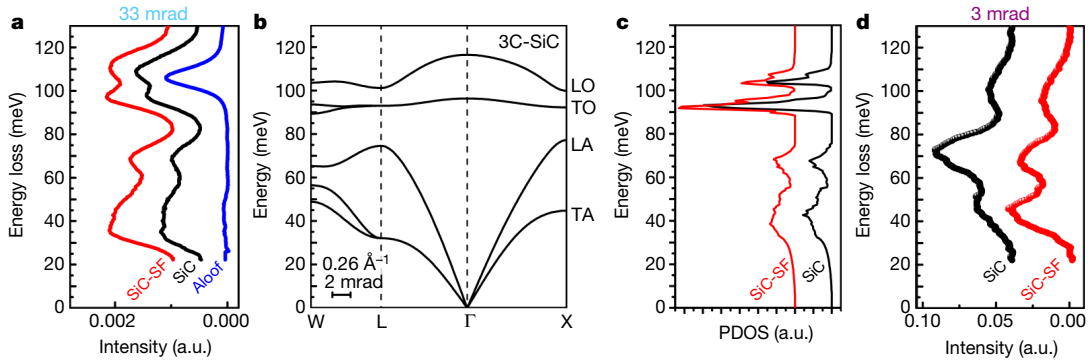


**Fig. 2 | Vibrational spectra of SiC with and without a stacking fault and taken with wide and narrow momentum ranges.** The momentum range is selected by the use of different aperture settings. **a**, Vibrational spectra of defect-free SiC (black curve), SiC with a stacking fault (SiC-SF, red curve) and the aloof signal (see main text; blue curve) with a probe convergence semi-angle of 33 mrad. The locations of the electron beam for acquiring these spectra are marked in Extended Data Fig. 1d. **b**, Simulated phonon dispersion curves of bulk 3C-phase SiC (3C-SiC). **c**, Simulated local phonon density of states (PDOS) of SiC with a stacking fault and of defect-free SiC. **d**, Angle-resolved vibrational spectra of defect-free SiC (black) and of SiC with a stacking fault (red) with a convergence semi-angle of 3 mrad at the X point.

assigned to the LO and TO modes respectively, while the third sharp peak at 68.5 meV and the broad low-energy peak in the energy range 30–50 meV are likely to be LA and TA modes respectively. Because the 33-mrad probe condition involves electron scattering in the entire BZ, as shown in the dashed red circle in Fig. 1d, the acquired vibrational spectrum is an average signal of all momentum exchanges, and is thus different from spectra acquired at the BZ centre by optical methods.

Under the 'aloof' condition (when the electron beam is placed outside the sample), only very small momentum exchanges take place, and the vibrational spectrum has a single peak at 106 meV. The energy is slightly different compared to the archetypal surface phonon polariton at 117.6 meV in 3C-phase SiC, but it is in good agreement with a surface phonon energy modified by sample thickness and morphology[38,41,42]. The vibrational signal from polar materials detected under the aloof condition is the surface phonon polariton, and arises from dipole scattering due to the coupling between the electromagnetic field generated by the electron beam and phonon resonances at the sample surface[27,29,32,41]. The aloof signal overlaps with the LO mode in spectra acquired inside the sample, and it broadens and red-shifts the LO peak from the standard value. The acoustic phonon modes are more localized and do not induce any polaritons because acoustic phonon branches do not intersect with the energy–momentum relation of fast electrons in reciprocal space (Extended Data Fig. 3). The remarkable difference of the vibrational spectra between the defect-containing region and the defect-free region occurs in the energy range 30–50 meV, where the TA modes of the stacking fault become stronger than those in the defect-free crystal region (Fig. 2a). Similar phenomena were observed when using a convergence semi-angle of 10 mrad (1.3 Å$^{-1}$) and collecting almost all phonon branches in the FBZ (Extended Data Fig. 4). Figure 2c shows simulation results of the spatially resolved phonon density of states (PDOS) from both the stacking fault and the defect-free region (see details in Methods and Extended Data Fig. 5). The simulated PDOS curves generally match the experimental angle-integrated vibrational spectra in Fig. 2a and reproduce the intensity enhancement in the energy range 30–50 meV at the stacking fault, which is consistent with experimental observation. Therefore, we suggest that the vibrational signal acquired with a large convergence semi-angle is comparable with the PDOS integrated in the FBZ[43].

To validate the local PDOS change at the stacking fault, and to determine the spatial width of the fault's phonon resonance, we performed two-dimensional (2D) phonon mapping. Figure 3a shows a 2D map of the integrated vibrational signal in the energy range 30–50 meV (the TA mode) in the area containing a stacking fault (Extended Data Fig. 1e). The enhancement of TA mode intensity at the stacking fault is unambiguous. The line profile in Fig. 3b indicates that the intensity of the TA mode approximates a Gaussian distribution centred at the stacking fault and with a peak width of 3.0 ± 0.6 nm. The average ADF STEM intensity also shows a 2.4-nm broadening in Fig. 3b, much like the variation of the TA mode intensity. This might be caused by the increased population of softened acoustic phonons at the stacking fault, which leads to additional thermal diffuse scattering for electrons and hence a stronger ADF intensity. A similar circumstance has recently

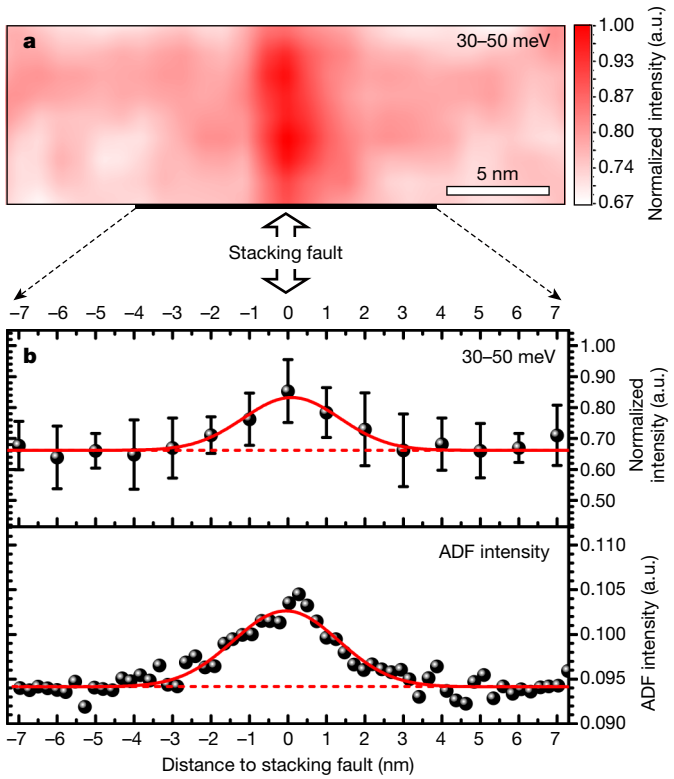


**Fig. 3 | High-spatial-resolution mapping of acoustic phonon enhancement.** **a**, Mapping of the vibrational signal integrated in the energy range of 30–50 meV across the stacking fault with a convergence semi-angle of 33 mrad. Colour scale shows the integrated signal intensity normalized by its maximum value. **b**, Line profile of the 30–50 meV signal (top) and the ADF intensity (bottom). The two superimposed red curves are Gaussian-type peak fittings. Error bars in top panel, standard deviation. The ADF intensity is averaged from the atomic-resolution STEM image (Extended Data Fig. 1e, f).

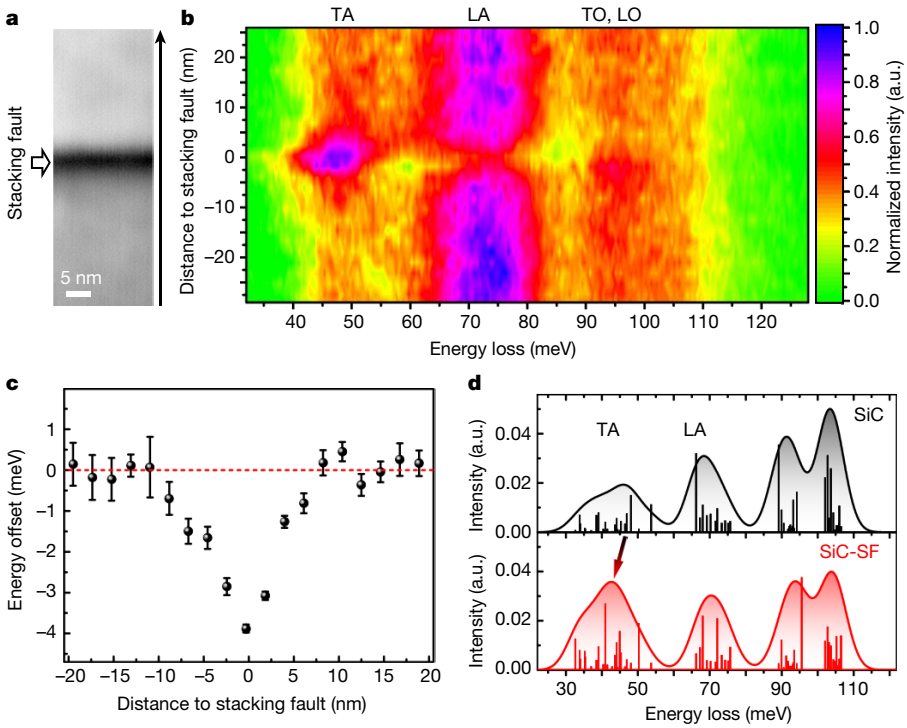


**Fig. 4 | Spatial distribution of individual phonon modes and the red energy shift of local phonon resonances under the angle-resolved condition.** **a**, ADF STEM image with a convergence semi-angle of 3 mrad. **b**, Line profile of the angle-resolved vibrational spectra at the X point of the FBZ across the stacking fault in the direction denoted by the black arrow in **a**. Colour scale shows the signal intensity normalized by its maximum. **c**, Energy offset of the 40–50 meV peak. Peak positions were determined by a peak fitting process, and the energy value of the TA mode (49 meV) in the defect-free SiC was subtracted, to obtain the numerical value of the energy offset. Error bars represent the fitting error of the peak centre of the TA mode. **d**, Simulated angle-resolved vibrational spectra of defect-free SiC (top, black) and of SiC with a stacking fault (bottom, red). The simulated structure was the same as shown in Extended Data Fig. 5a. Defect-free and stacking-fault regions were selected as layer one (L01, at the bottom), and layer seven (L07, in the middle) in this structure, respectively. Bars represent the mode-resolved calculated intensities, which were then broadened with a Gaussian peak with 8 meV FWHM, resulting in the curves. The arrow represents the energy shift of the maximal point of TA modes on going from defect-free SiC to SiC with a stacking fault.

been reported elsewhere[44], suggesting that acoustic phonon intensity correlates with edge or defect structures, whereas optical phonons are more sensitive to the local thickness.

In order to clarify the origin of the acoustic phonon enhancement, spectra were acquired with a 3-mrad convergence semi-angle and a 2.5-mrad EELS collection semi-angle, so as to achieve better momentum resolution (0.5 $Å^{-1}$). A spatial resolution of about 2.6 nm, as highlighted by the purple bar in Fig. 1b, was achieved in this condition. The different phonon branches in an energy–momentum ($E$–$q$) diagram then become clearly separated (Extended Data Fig. 6), and the stacking fault of Fig. 1c is spatially resolved in both the ADF and the phonon signals, as shown in Fig. 4a. The spatial mapping of Fig. 4b can be usefully compared with angle-resolved spectra recorded at the X point, and shown in Fig. 2d. The high-symmetry X point was selected because both LA and TA branches reach their maximal values there (together with the occurrence of the van Hove singularity, ensuring sufficient EELS signal, Fig. 2b, c) and are well separated from each other, which both make the signal identification easy. For the defect-free SiC crystal, the LO and TO branches are located at 104 meV and 94 meV respectively after peak separation and the LA and TA branches are at 73 meV and 49 meV respectively. These values agree with the peak locations in the simulated phonon dispersion curves of Fig. 2b. The small offsets of LA and TA modes probably come from the steep branches and the momentum uncertainty (±0.5 $Å^{-1}$). The phonon dispersion relation was further examined by performing angle-resolved vibrational spectroscopy along the X–Γ′ direction, and the measured results are in good agreement with simulated phonon bands of SiC (Extended Data Fig. 6c). In comparison with the aloof spectrum acquired at the Γ point, no obvious polariton signal was recorded in the aloof condition at the X point (Extended Data Fig. 6d), suggesting that the off-axis condition can exclude the polariton mode.

Compared to the angle-integrated spectra of Fig. 2a, the angle-resolved vibrational spectra of Fig. 2d show more noticeable differences between acoustic phonons of perfectly crystalline and defect-containing structures. In particular, the intensities of the LA and TA modes are strongly modulated by the stacking fault, which weakens the LA and enhances the TA mode. This can also be seen in the spectrum map of Fig. 4b, which further suggests that the TO and LO modes remained unchanged. Figure 4c shows the energy offset of the TA mode in the 40–50 meV region, with a maximum red shift of 3.8 meV. The systematic error of the peak fitting algorithm is 0.1–0.6 meV, and the red shift is therefore much larger than the measurement error. Meanwhile, the energy of the LA mode of the stacking fault was also reduced by 3 meV compared to defect-free SiC.

The effect of a stacking fault in SiC can be simulated in the framework of density functional theory (DFT) by inserting two atomic planes of the 2H-SiC polytype into a 3C-SiC structure (Extended Data Fig. 5a). Figure 4d plots the angle-resolved and site-specific vibrational spectra taking into account the scattering probability of fast electrons[44] (see more details in Methods). The peak position of the TA mode in the DFT spectrum undergoes a red energy shift of 3.8 meV from defect-free SiC (46.4 meV) to stacking-fault-containing (42.6 meV) regions, which is consistent with the experimental angle-resolved vibrational spectroscopy in Fig. 4c. Meanwhile, simulation results also reproduced the intensity modulation of both TA and LA modes in the experimental data. Separated local PDOS results reveal that enhanced local modes at the stacking fault between 30 meV and 50 meV include vibrations along directions both normal and parallel to the plane of the stacking fault (Extended Data Fig. 7). We can deduce that symmetry breaking and variation of interatomic force constants lead to the shift of vibration energy at the stacking fault in the energy range 30–50 meV; this shift appears in the same energy range as the TA modes of bulk SiC.

A more direct comparison between phonon bands of the 3C-phase SiC and the stacking-fault-like 2H-phase SiC also supports the occurrence of defect phonons due to different local atomic arrangements. The dispersion relations of the 2H polytype, shown in Extended Data Fig. 8, has additional branches near 40 meV at the X point. The theoretical energy position of each phonon mode of defect-free and stacking-fault SiC structures at the X point also reproduced the red shifts of both TA and LA modes at the stacking fault as observed in experiments (Extended Data Fig. 8d). The enhanced intensity in the 40–50 meV energy region and the associated red shift at the stacking fault can be readily correlated with the additional branches. The defect-induced phonon branch behaves like an optical one, with nearly zero group velocity (Extended Data Fig. 8c). Additionally, the local vibrational spectrum of the stacking

fault at the Δ point (half-way between the Γ and X points) constitutes a broad signal in the energy range 30–80 meV rather than two noticeable peaks at about 56 meV and 34 meV as in the spectrum of the defect-free region (Extended Data Fig. 8e). This discrepancy implies the presence of defect modes at the stacking fault as well. The above analysis indicates that the defect-containing region impedes thermal transport and reduces local phonon propagation. This may potentially lead to a defect-induced reduction in the thermal conductivity[13,34].

The propagation width of the local phonon resonance is further revealed by the variation of the vibrational signal. Under the small-convergence-angle condition, the line profile of the signal integrals of 45–50 meV and 70–75 meV (Extended Data Fig. 9a) both present a full-width at half-maximum (FWHM) of 6.8 ± 0.7 nm, centred on the stacking fault. The line profile of the energy offset of TA modes in Fig. 4b has an FWHM of 7.8 nm. All these widths are considerably larger than the spatial resolution of about 2.6 nm, achieved for the 3-mrad convergence semi-angle condition. This indicates that the correct width of the stacking fault's phonons has been measured, and that it is wider than the structural width of the stacking fault (0.25 nm). The increased width can be explained by the penetration of the red-shifted local phonon into the surrounding SiC region, even though strictly speaking it is forbidden there in the classical picture. According to the one-dimensional Schrödinger equation, the decay of the local defect phonon mode near the stacking fault scales with the inverse of the square root of the energy difference between the red-shifted defect mode and the original TA mode in defect-free SiC (3.8 meV here, see Extended Data Fig. 9b). Simulation with the real-space Green's function approach for a larger structure also indicates that the stacking fault causes the red energy shift of the TA modes of surrounding atoms (Extended Data Fig. 10).

We have experimentally observed defect-induced local phonon resonances and an associated red energy shift by using a combination of atomic resolution and angle-resolved EELS. Our method opens up the possibility of studying the local vibrational signal at structural and substitutional defects in materials. We expect it to find important applications in many different areas, ranging from the study of thermal-resistance-inducing interfacial phonons to defect structures engineered to optimize a material's thermal properties. This experimental capability could potentially be used to reveal the local phonon spectral density at point defects in bulk crystals[6] with further improvement of signal filtering.

## Online content

Any methods, additional references, Nature Research reporting summaries, source data, extended data, supplementary information, acknowledgements, peer review information; details of author contributions and competing interests; and statements of data and code availability are available at https://doi.org/10.1038/s41586-020-03049-y.


1. Krumhansl, J. A. Lattice vibrations in solids. *J. Appl. Phys.* **33**, 307–319 (1962).
2. Li, M. D. et al. Nonperturbative quantum nature of the dislocation phonon interaction. *Nano Lett.* **17**, 1587–1594 (2017).
3. Walker, C. T. & Pohl, R. O. Phonon scattering by point defects. *Phys. Rev.* **131**, 1433–1442 (1963).
4. Katcho, N. A., Carrete, J., Li, W. & Mingo, N. Effect of nitrogen and vacancy defects on the thermal conductivity of diamond: an ab initio Green's function approach. *Phys. Rev. B* **90**, 094117 (2014).
5. Klemens, P. G. The scattering of low-frequency lattice waves by static imperfections. *Proc. Phys. Soc. A* **68**, 1113–1128 (1955).
6. Katre, A., Carrete, J., Dongre, B., Madsen, G. K. H. & Mingo, N. Exceptionally strong phonon scattering by B substitution in cubic SiC. *Phys. Rev. Lett.* **119**, 075902 (2017).
7. Singh, B. K., Menon, V. J. & Sood, K. C. Phonon conductivity of plastically deformed crystals: role of stacking faults and dislocations. *Phys. Rev. B* **74**, 184302 (2006).
8. Ohashi, K. & Ohashi, Y. Mean-square displacement of a vibrating dislocation. *Phil. Mag. A* **38**, 187–204 (1978).
9. Pernot, G. et al. Precise control of thermal conductivity at the nanoscale through individual phonon-scattering barriers. *Nat. Mater.* **9**, 491–495 (2010).
10. Huberman, S. et al. Observation of second sound in graphite at temperatures above 100 K. *Science* **364**, 375–379 (2019).
11. Lindsay, L., Katre, A., Cepellotti, A. & Mingo, N. Perspective on ab initio phonon thermal transport. *J. Appl. Phys.* **126**, 050902 (2019).
12. Arrigoni, M., Carrete, J., Mingo, N. & Madsen, G. K. H. First-principles quantitative prediction of the lattice thermal conductivity in random semiconductor alloys: the role of force-constant disorder. *Phys. Rev. B* **98**, 115205 (2018).
13. Carrete, J. et al. Phonon transport across crystal-phase interfaces and twin boundaries in semiconducting nanowires. *Nanoscale* **11**, 16007–16016 (2019).
14. Sheng, P. *Introduction to Wave Scattering, Localization and Mesoscopic Phenomena* (Springer Series in Materials Science Vol. 88, Springer, 2006).
15. McCreery, R. L. *Raman Spectroscopy for Chemical Analysis* (Chemical Analysis: a Series of Monographs on Analytical Chemistry and its Applications Vol. 157, Wiley, 2000).
16. Bechelany, M., Brioude, A., Cornu, D., Ferro, G. & Miele, P. A Raman spectroscopy study of individual SiC nanowires. *Adv. Funct. Mater.* **17**, 939–943 (2007).
17. Stuart, B. *Infrared Spectroscopy: Fundamentals and Applications* (Wiley, 2004).
18. Chan, K. L. A. & Kazarian, S. G. New opportunities in micro- and macro-attenuated total reflection infrared spectroscopic imaging: spatial resolution and sampling versatility. *Appl. Spectrosc.* **57**, 381–389 (2003).
19. Maciel, I. O. et al. Electron and phonon renormalization near charged defects in carbon nanotubes. *Nat. Mater.* **7**, 878–883 (2008).
20. Burkel, E. Phonon spectroscopy by inelastic x-ray scattering. *Rep. Prog. Phys.* **63**, 171–232 (2000).
21. Mitchell, P. C. H. *Vibrational Spectroscopy with Neutrons: with Applications in Chemistry, Biology, Materials Science and Catalysis* Vol. 3 (World Scientific, 2005).
22. Stipe, B. C., Rezaei, M. A. & Ho, W. Single-molecule vibrational spectroscopy and microscopy. *Science* **280**, 1732–1735 (1998).
23. Altfeder, I. et al. Scanning tunneling microscopy observation of phonon condensate. *Sci. Rep.* **7**, 43214 (2017).
24. Krivanek, O. L. et al. Vibrational spectroscopy in the electron microscope. *Nature* **514**, 209–212 (2014).
25. Hachtel, J. A. et al. Identification of site-specific isotopic labels by vibrational spectroscopy in the electron microscope. *Science* **363**, 525–528 (2019).
26. Hage, F., Kepaptsoglou, D., Ramasse, Q. & Allen, L. Phonon spectroscopy at atomic resolution. *Phys. Rev. Lett.* **122**, 016103 (2019).
27. Lagos, M. J., Trügler, A., Hohenester, U. & Batson, P. E. Mapping vibrational surface and bulk modes in a single nanocube. *Nature* **543**, 529–532 (2017).
28. Govyadinov, A. A. et al. Probing low-energy hyperbolic polaritons in van der Waals crystals with an electron microscope. *Nat. Commun.* **8**, 95 (2017).
29. Venkatraman, K., Rez, P., March, K. & Crozier, P. A. The influence of surfaces and interfaces on high spatial resolution vibrational EELS from $SiO_2$. *Microscopy* **67**, i14–i23 (2018).
30. Hage, F. S. et al. Nanoscale momentum-resolved vibrational spectroscopy. *Sci. Adv.* **4**, eaar7495 (2018).
31. Rez, P. et al. Damage-free vibrational spectroscopy of biological materials in the electron microscope. *Nat. Commun.* **7**, 10945 (2016); erratum **7**, 11592 (2016).
32. Dwyer, C. et al. Electron-beam mapping of vibrational modes with nanometer spatial resolution. *Phys. Rev. Lett.* **117**, 256101 (2016).
33. Lindefelt, U., Iwata, H., Öberg, S. & Briddon, P. R. Stacking faults in 3C-, 4H-, and 6H-SiC polytypes investigated by an ab initio supercell method. *Phys. Rev. B* **67**, 155204 (2003).
34. Goela, J. S., Brese, N. E., Burns, L. E. & Pickering, M. A. in *High Thermal Conductivity Materials* (eds Shindé, S. L. & Goela, J. S.) 167–198 (Springer, 2006).
35. Yamasaki, J., Inamoto, S., Nomura, Y., Tamaki, H. & Tanaka, N. Atomic structure analysis of stacking faults and misfit dislocations at 3C-SiC/Si(001) interfaces by aberration-corrected transmission electron microscopy. *J. Phys. D* **45**, 494002 (2012).
36. Stevens, R. Defects in silicon carbide. *J. Mater. Sci.* **7**, 517–521 (1972).
37. Williams, D. B. & Carter, C. B. *Transmission Electron Microscopy: a Textbook for Materials Science* Vol. 2 (Springer Science & Business Media, 2009).
38. Nienhaus, H., Kampen, T. U. & Mönch, W. Phonons in 3C-SiC, 4H-SiC, and 6H-SiC. *Surf. Sci.* **324**, L328–L332 (1995).
39. Serrano, J. et al. Determination of the phonon dispersion of zinc blende (3C) silicon carbide by inelastic X-ray scattering. *Appl. Phys. Lett.* **80**, 4360–4362 (2002).
40. Strauch, D. et al. Phonons in SiC from INS, IXS, and ab-initio calculations. *Mater. Sci. Forum* **527–529**, 689–694 (2006).
41. Yan, X. et al. Unexpected strong thermally induced phonon energy shift for mapping local temperature. *Nano Lett.* **19**, 7494–7502 (2019).
42. Lourenço-Martins, H. & Kociak, M. Vibrational surface electron-energy-loss spectroscopy probes confined surface-phonon modes. *Phys. Rev. X* **7**, 041059 (2017).
43. Venkatraman, K., Levin, B. D. A., March, K., Rez, P. & Crozier, P. A. Vibrational spectroscopy at atomic resolution with electron impact scattering. *Nat. Phys.* **15**, 1237–1241 (2019).
44. Senga, R. et al. Position and momentum mapping of vibrations in graphene nanostructures. *Nature* **573**, 247–250 (2019).

# Methods

### Experimental details

The cross-sectional SiC specimen was prepared from a 3C-phase SiC film grown on a Si(001) wafer by mechanical thinning and polishing followed by an ion milling process. The vibrational spectra were acquired by a Nion UltraSTEM 200 equipped with a C3/C5 aberration corrector and a high-energy-resolution monochromated EELS system (HERMES). The instrument was operated at 60 kV with convergence semi-angles ($\alpha$) varied from 1 mrad to 33 mrad. As marked in Fig. 1b, the spatial resolution enabling identification of the stacking fault can only be acquired when $\alpha \geq 22$ mrad, while the momentum resolution allowing for the separation of the Γ and X points can be obtained when $\alpha \leq 5.5$ mrad (half of the reciprocal distance between Γ and X). For STEM imaging, the inner and outer collection semi-angles of high-angle and medium-angle annular dark-field (HAADF and MAADF) detectors were 70–210 mrad and 40–70 mrad, respectively. STEM image simulation was carried out using a multislice based simulation software called QSTEM with experimental parameters[45]. To obtain an adequate vibrational signal, the beam current was fixed at ~120 pA for all conditions. An alpha-type monochromator was activated and carefully tuned to achieve the best energy resolution of 5.7 meV. For angle-resolved vibrational spectroscopy, the post-specimen tilting method was used to shift the diffraction plane through projector lens and allowed scattered electrons at different momenta to pass through the EELS entrance aperture. The post-specimen tilting method is more convenient than the pre-specimen tilting one, which requires tilting the beam and re-orienting the sample again[32]. The collection semi-angle for EELS acquisition was 2.5 mrad obtained by inserting a 0.2-mm EELS entrance aperture and properly adjusting the strength of the projection lens. The EELS dispersion was about 0.5 meV per channel which was routinely calibrated by wobbling the zero-loss peak (ZLP) at a high frequency with a known amplitude of voltage through the drift tube. The ZLP in vacuum was acquired with 5-ms exposure time to demonstrate the best energy resolution performance. To optimize the signal-to-noise ratio and maximize high tension stability, single EEL spectra were acquired by summing 100–200 frames with 1 s exposure per frame, which were then all aligned by the centre of the ZLP. High-spatial-resolution vibrational mapping and line-scan data were acquired by running our custom python script in Nion's Swift software. The code combines functions of automatically controlling the electron probe position, correcting sample drift, tuning low-order EELS aberrations, acquiring vibrational spectra, aligning the ZLP of multiple spectra per point, and finally exporting the summed spectra. Each spectrum in the map data was acquired by summing a few frames of 1-s exposures per point, while summing several tens of frames of 1-s exposures per point was used for the line-scan data. Restricting the total acquisition time to 1 h ensures an adequate probe current and reduces the influence of sample drift. The pixel size was 0.75–2 nm to match different fields of view. Background subtraction was then performed by fitting an exponential polynomial function[27]. Peak separation was performed by fitting multiple Gaussian-type peaks[41].

### DFT simulation

The first-principles calculations were performed based on density functional theory (DFT) by the Vienna ab initio simulation package (VASP)[46,47]. A Perdew–Burke–Ernzerhof functional with the projector-augmented-wave method[48] was used in all simulations. We took the 4 × 4 × 4 supercell of 3C-phase SiC, the 3 × 3 × 3 supercell of 2H-phase SiC and the 3 × 3 × 1 supercell of the 11-layer defect structure as shown in Extended Data Fig. 8a, b and Extended Data Fig. 5a, respectively. The lattice constants for the 3C phase, the 2H phase and defect structures are $a = b = c = 12.38$ Å, $a = b = 9.27$ Å, $c = 15.21$ Å, and $a = b = 9.28$ Å, $c = 27.81$ Å, respectively. These models were fully relaxed with Hellmann–Feynman forces less than $1 \times 10^{-5}$ eV Å$^{-1}$ and electronic convergence less than $1 \times 10^{-4}$ eV. The energy cutoff for the basis expansion was 460 eV, and the $k$ points were sampled with a 3 × 3 × 3 mesh for 3C phase, a 3 × 3 × 2 mesh for 2H phase and a 4 × 4 × 1 mesh for the 11-layer defect structure in their corresponding BZs[49]. The phonopy code[50] was run to analyse the phonon dispersions and density of states with density functional perturbation theory (DFPT)[51] as implemented in VASP. Dielectric tensor and Born effective charge were used to modify the longitudinal optical–transverse optical (LO–TO) splitting for 3C and 2H phases. For the defect structure, the projected PDOS in Extended Data Fig. 5b was calculated by adding all density of states of the atoms in individual layers. We further used the expression for Stokes cross-section to calculate the scattering probability of fast electrons[44,52]. Specific atoms ($I$) in either defect-free SiC or the stacking-fault region of the 11-layer defect structure were selected to separate the contribution from defects. The momentum exchange ($\mathbf{q}$) was taken into account as well. To match the experimental condition of the X point of 3C-phase SiC, the X″ point was selected in the FBZ of the large supercell as shown in Extended Data Fig. 5c. In order to obtain the effective change $\mathbf{Z}_I(\mathbf{q})$, we calculated the response of valence-electron-density $\Delta n_{I,\upsilon}(\mathbf{q})$ to atomic displacements in the $\upsilon$ direction of $I$ ions through following steps. (1) We constructed 3$N$ phonon branches ($N$ is the number of atoms in the supercell) with atoms being displaced according to the phonon eigenvectors at $\mathbf{q}$. (2) We obtained wavefunctions and charge densities of all phonon branches from the first-principles calculations. The differences of valence charge densities between models with atomic displacements and with no displacement were extracted and integrated to obtain the charge redistributions of all 3$N$ vibrational modes, $\Delta n_{3N}(\mathbf{q})$. With 22 atoms in the supercell (see Extended Data Fig. 7a), there are in total 66 phonon branches, resulting in 66 non-zero modes at the X″ point. Finally, $\Delta n_{3N}(\mathbf{q})$ values were converted to $\Delta n_{I,\upsilon}(\mathbf{q})$ by projecting the eigenvector in atom $I$ and direction $\upsilon$. Plugging the effective charge into the expression for scattering probability, vibrational spectra were simulated for selected atoms and momentum exchange as shown in Fig. 4d.

### Spatial resolution

The size of the electron probe on the sample is commonly defined as $d_r = (d_g^2 + d_s^2 + d_d^2)^{0.5}$, where $d_g$, $d_s$ and $d_d$ represent the beam source size, broadening of the spherical aberration and the diffraction limit, respectively[37]. The contribution of spherical aberration can be neglected owing to the implementation of the aberration corrector. Then, the spatial resolution is estimated by the following relationship with convergence semi-angle $\alpha$ as $d_r = (d_g^2 + d_d^2)^{0.5} = \{[(2/\pi)(I_p/B)^{0.5}(1/\alpha)]^2 + (1.22\lambda/\alpha)^2\}^{0.5} = f(I_p, \lambda)/\alpha$, where $I_p$ is the probe current, $B$ is the source brightness, $\lambda$ is the wavelength of the electron, and $f(I_p, \lambda)$ is a function independent of $\alpha$. In order to achieve the best signal-to-noise ratio, the probe current ($I_p$) was fixed at the maximal value, which involves a non-negligible source size ($d_g$) and causes the measured probe size to be greater than the diffraction-limited resolution. With $\lambda$ as a constant at the fixed accelerating voltage of 60 kV, $d_r$ is inversely proportional to $\alpha$ and the experimental measurement in Fig. 1b is consistent with this trend.

### Momentum resolution

Momentum resolution ($m_r$) is defined as the convolution of the convergence semi-angle with the size of the EELS entrance aperture (collection semi-angle, $\beta$), as $m_r = (\alpha^2 + \beta^2)^{0.5}$ (ref. [30]). The value of $m_r$ is reduced as $\alpha$ decreases, as shown in Fig. 1b.

### Energy resolution

After the implementation of the drift tube in the spectrometer, the energy dispersion was precisely calibrated, thus providing the best energy resolution of 5.7 ± 0.5 meV under 60 keV in our instrument. The energy resolution ($E_r$) is defined as the FWHM of the ZLP, which is an energy-dispersed image of the EELS entrance crossover, formed

in the back-focal plane of the last projector lens of the microscope[24]. The entrance crossover is an image of the sample-level probe, which grows larger when the convergence angle becomes smaller, as shown in the bottom half of Fig. 1b. If the microscope post-specimen optics and EELS optics are kept the same when the electron beam convergence angle decreases, the probe becomes larger and, thus, the corresponding increase in the EELS entrance crossover size produces an increase in the width of the ZLP at the EELS detector and hence worse energy resolution, as shown in the top part of Fig. 1b. One can overcome this by changing the post-sample optics to keep the size of the EELS entrance crossover the same even as the probe size at the sample grows, but this makes the set-up more complicated.

## Data availability

The datasets generated during and/or analysed during the current study are available from the corresponding authors on reasonable request.


45. Koch, C. T. *Determination of Core Structure Periodicity and Point Defect Density along Dislocations*. DPhil thesis, Arizona State University (2002).
46. Kresse, G. & Hafner, J. Ab initio molecular dynamics for liquid metals. *Phys. Rev. B* **47**, 558–561 (1993).
47. Kresse, G. & Hafner, J. Ab initio molecular-dynamics simulation of the liquid-metal amorphous-semiconductor transition in germanium. *Phys. Rev. B* **49**, 14251–14269 (1994).
48. Kresse, G. & Joubert, D. From ultrasoft pseudopotentials to the projector augmented-wave method. *Phys. Rev. B* **59**, 1758–1775 (1999).
49. Monkhorst, H. J. & Pack, J. D. Special points for Brillouin-zone integrations. *Phys. Rev. B* **13**, 5188–5192 (1976).
50. Togo, A., Oba, F. & Tanaka, I. First-principles calculations of the ferroelastic transition between rutile-type and $CaCl_2$-type $SiO_2$ at high pressures. *Phys. Rev. B* **78**, 134106 (2008).
51. Gonze, X. & Lee, C. Dynamical matrices, Born effective charges, dielectric permittivity tensors, and interatomic force constants from density-functional perturbation theory. *Phys. Rev. B* **55**, 10355–10368 (1997).
52. Giannozzi, P., de Gironcoli, S., Pavone, P. & Baroni, S. Ab initio calculation of phonon dispersions in semiconductors. *Phys. Rev. B* **43**, 7231–7242 (1991).
53. Henry, C. H. & Hopfield, J. J. Raman scattering by polaritons. *Phys. Rev. Lett*. **15**, 964–966 (1965).
54. García de Abajo, F. L. Optical excitations in electron microscopy. *Rev. Mod. Phys*. **82**, 209–275 (2010).
55. Wang, T., Carrete, J., van Roekeghem, A., Mingo, N. & Madsen, G. K. H. Ab initio phonon scattering by dislocations. *Phys. Rev. B* **95**, 245304 (2017).



**Acknowledgements** The experimental work was supported by the Department of Energy (DOE), Office of Basic Energy Sciences, Division of Materials Sciences and Engineering under grant DESC0014430. DFT studies were supported by the US Department of Energy (grant no. DE-FG02-05ER46237) and the National Energy Research Scientific Computing Center (NERSC). This research was partially supported by the NSF through the University of California-Irvine Materials Research Science and Engineering Center (grant no. DMR-2011967). We thank Z. Cheng and S. Graham (Georgia Institute of Technology) and Q. Ramasse (SuperSTEM Laboratory) for their constructive suggestions. TEM experiments were conducted using the facilities in the Irvine Materials Research Institute (IMRI) at the University of California, Irvine.


**Author contributions** X.Y., R.W. and X.P. conceived this project and designed the studies. X.Y. performed STEM-EELS experiments. X.Y. and C.A.G. analysed EELS data. C.L., L.G. and R.W. designed and performed the theoretical simulations. T.A., T.C.L., N.D. and O.L.K. set up the angular resolved condition with high-energy-resolution EELS. The SiC films were provided by D.G.S. All authors discussed and commented on the results. The manuscript was prepared by X.Y., C.L., C.A.G., O.L.K., R.W. and X.P., with contributions from all other co-authors.

**Competing interests** T.C.L., N.D. and O.L.K. declare a financial interest in Nion Company.


**Additional information**
**Correspondence and** requests for materials should be addressed to R.W. or X.P.
**Peer review information** *Nature* thanks Kazu Suenaga and the other, anonymous, reviewer(s) for their contribution to the peer review of this work.
**Reprints and permissions information** is available at http://www.nature.com/reprints.

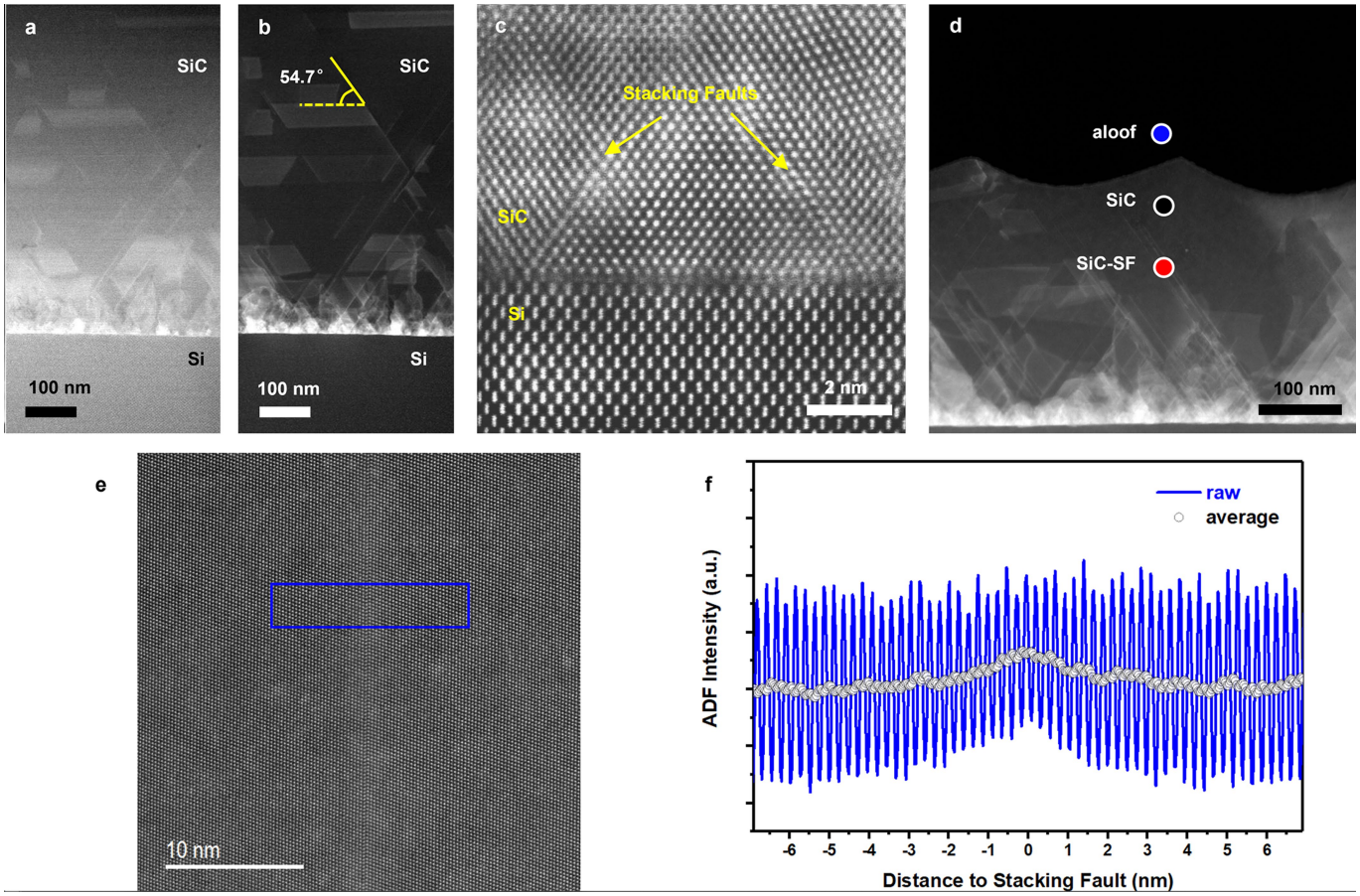


**Extended Data Fig. 1 | STEM observations of 3C-phase SiC showing stacking faults.** The SiC was grown on a Si(001) wafer. **a**, **b**, High-angle (**a**) and medium-angle (**b**) ADF-STEM of SiC along [01$\bar{1}$]. The medium-angle condition is more sensitive to the defect structure, owing to the contribution of diffraction contrast, and hence the stacking faults and other defects have a stronger contrast in **b**. The SiC film was epitaxially grown on an (001) plane of the Si wafer. The stacking faults form along the <111> direction with angles of 54.7° with respect to the interface between SiC and Si. **c**, Atomic-resolution high-angle ADF-STEM image of the SiC–Si interface along [01$\bar{1}$]. Owing to the large lattice mismatch of 24.5% between film and substrate ($a_{SiC}$ = 0.543 nm and $a_{Si}$ = 0.436 nm), many structural defects, including multiple stacking faults (arrowed), are generated from the interface. **d**, Low-magnification medium-angle ADF-STEM image with marked electron beam locations for acquiring the aloof, SiC and SiC-SF vibrational spectra shown in main-text Fig. 2a. **e**, HAADF STEM image of one stacking fault with a large field of view acquired with a convergence semi-angle of 33 mrad and an ADF detector collection semi-angle of 70–210 mrad. **f**, Vertically integrated intensity profile along the blue box in **e**. The grey dots are average intensity and used in the line profile of the ADF intensity in main-text Fig. 3b. The average intensities of the atomic columns are uniform except the region near the stacking fault.

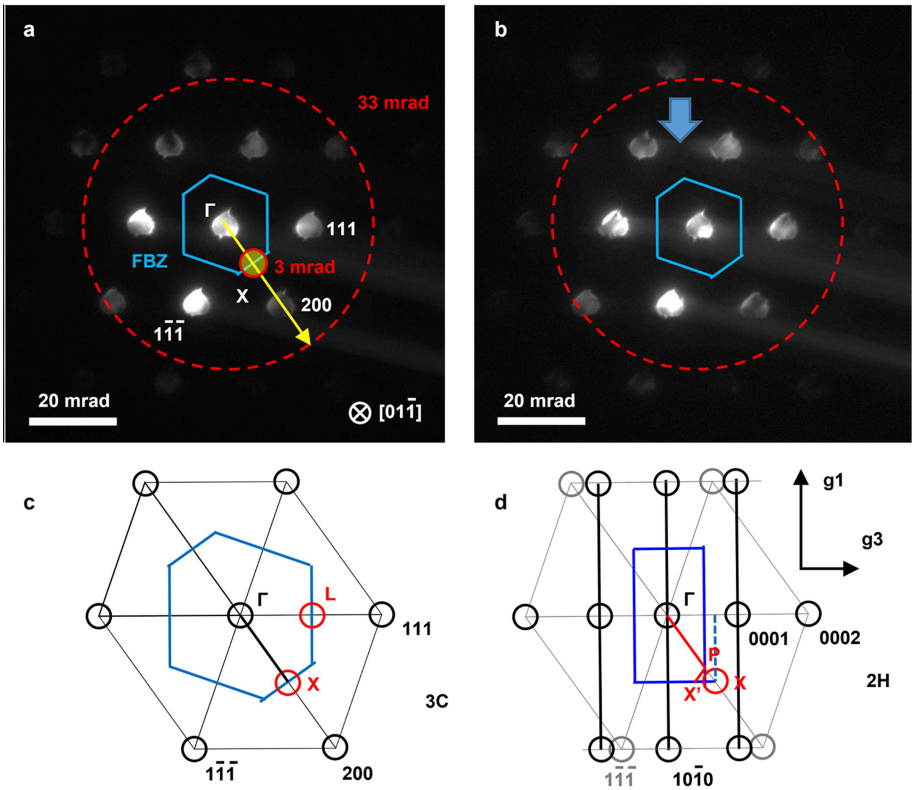


**Extended Data Fig. 2 | Relationship of the diffraction pattern and the FBZ in defect-free SiC and in a region containing a stacking fault. a**, **b**, Convergent beam diffraction patterns of defect-free SiC (**a**) and a stacking-fault region (**b**) taken with a 3 mrad convergence semi-angle. The additional diffuse scattering signal marked by the blue arrow in **b** is correlated with the stacking-fault structure and local symmetry breaking. **c**, **d**, Reciprocal space diagrams, including the diffraction pattern and the location of the FBZ (blue contours), corresponding to **a** and **b**, respectively. For the stacking fault, a 2H phase is used to simulate the phonon dispersion relations in **d**. Although the X point in 3C phase is outside the FBZ of 2H phase, an equivalent path to Γ–X is indicated by the red lines along Γ–P–X′, in which X′ is at the edge of the FBZ of the 2H-SiC structure and has coordinates of (1/2, 0, 2/3) in fractions of reciprocal lattice vectors ($\mathbf{g}_1$, $\mathbf{g}_2$, $\mathbf{g}_3$) of 2H phase. $\mathbf{g}_1$ and $\mathbf{g}_3$ are in-plane reciprocal lattice vectors and indicated as two arrows, while $\mathbf{g}_2$ is out-of-plane and not indicated here.

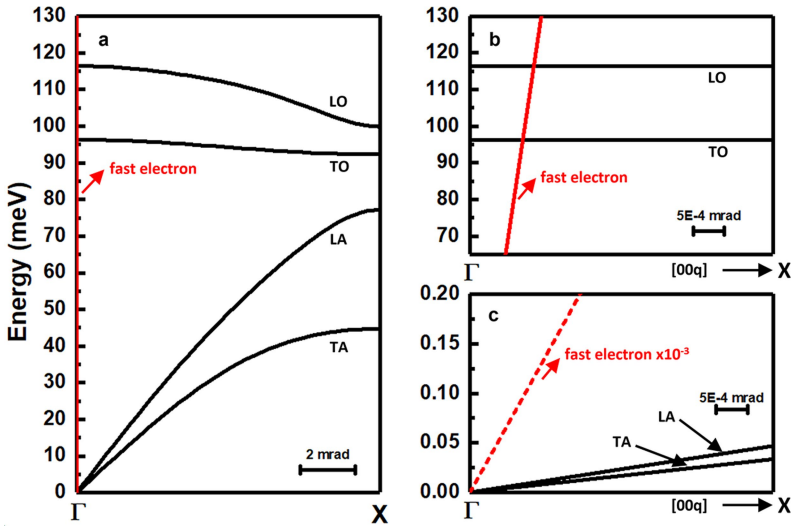


**Extended Data Fig. 3 | Interaction between the energy–momentum relation for fast electrons and the phonon dispersion curves of SiC. a**, The energy–momentum ($E$–$q$) relation for fast electrons (red line) along with the calculated phonon dispersion curves of 3C-phase SiC (black lines), which are duplicated from main-text Fig. 2b. The $E$–$q$ relation for fast electrons follows $E = \hbar v q$ in the long-wavelength range, where $\hbar$ is the reduced Planck constant and $v = 1.34 \times 10^8$ m s$^{-1}$ is the velocity of fast electrons for an accelerating voltage of 60 kV. Because the red line is near-vertical, we show in **b** and **c** enlarged sections of **a** for clarity. **b**, Enlarged plot to show intersections between the $E$–$q$ relation for fast electrons and the optical branches. [00$q$] denotes the direction towards the X point and parallel to [001] with a momentum of $q$. **c**, Enlarged plot of the corner of the Γ point with very small energy and momentum. To further clarify the $E$–$q$ relation for fast electrons at this small momentum, the energy is divided by 1,000 as indicated by the red dashed line. The polariton mode occurs when the $E$–$q$ relation of the fast electrons intersects the phonon dispersion curves[53,54]. Owing to the high speed of fast electrons, their $E$–$q$ relation is very close to the vertical line at the Γ point, and intersects with LO and TO branches (shown in **b**), but does not have any non-zero intersections with either LA or TA branches (as shown in **c**) because of their slow velocities ($9.5 \times 10^3$ m s$^{-1}$ and $4.1 \times 10^3$ m s$^{-1}$ for LA and TA in 3C-phase SiC, respectively).

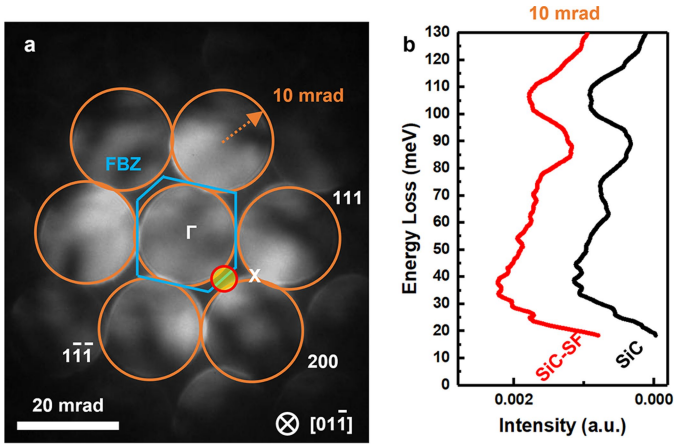


**Extended Data Fig. 4 | Vibrational spectra of defect-free SiC and of a region containing a stacking fault obtained using a convergence semi-angle ($\alpha$) of 10 mrad. a**, Diffraction pattern of defect-free SiC along the [01$\bar{1}$] direction with $\alpha$ = 10 mrad. The blue contour is the FBZ. 200, 111 and 1$\bar{1}\bar{1}$ diffraction spots are marked by orange circles with a radius of 10 mrad. The small red circle indicates the location of the EELS entrance aperture with a collection semi-angle of 2.5 mrad, which is at the X point to avoid the polariton mode. **b**, Vibrational spectra of defect-free SiC (black curve) and a stacking-fault-containing region (SiC-SF, red curve) with $\alpha$ = 10 mrad. Background-subtracted vibrational spectra in **b** are almost identical to the data obtained using 33 mrad in Fig. 2a. The TA signal (at 30–50 meV) in the spectrum of stacking-fault region is slightly stronger than that in the spectrum of the defect-free region, which is also consistent with the observed discrepancy using 33 mrad in Fig. 2a.

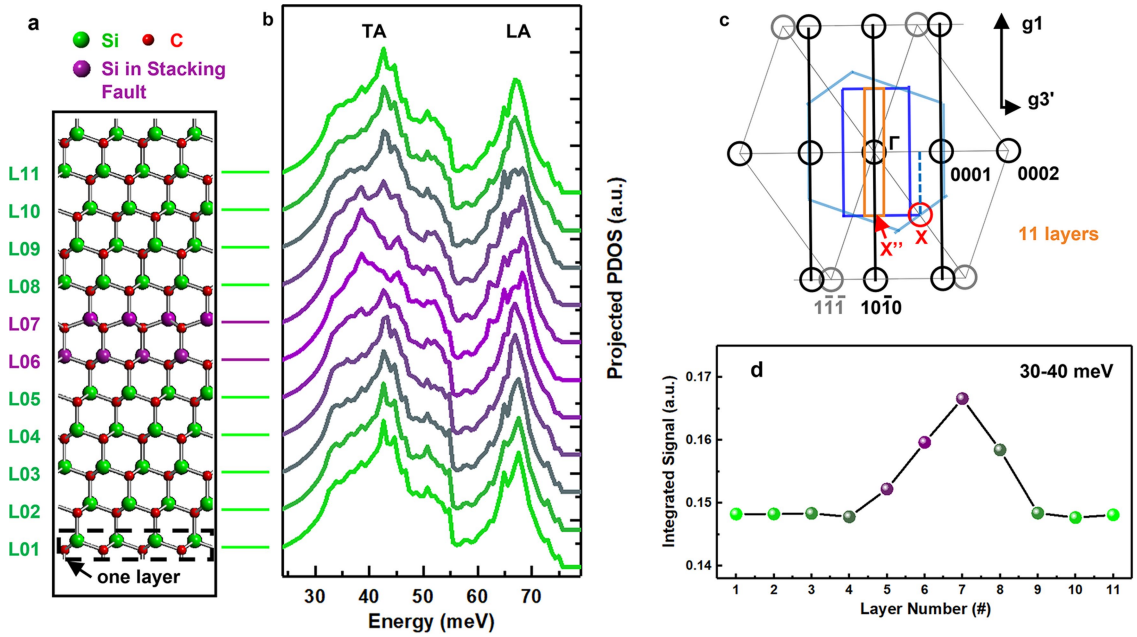


**Extended Data Fig. 5 | Spatially resolved simulation of projected PDOS across a stacking fault. a**, Eleven-layer atomic structure for the simulation, comprising 3C-phase SiC with a two-layer stacking fault (purple) in the middle. The number of each layer is given on the left-hand side. **b**, Projected PDOS plots corresponding to individual layers in the atomic structure. The two simulated spectra in main-text Fig. 2c are from the stacking fault (purple curve) and from the defect-free region (green curve). These results even reproduced the 4-meV red shift of the TA mode centre in the stacking fault. **c**, Reciprocal space diagram illustrating the location of the FBZ of the 11-layer defect structure in **a** (orange contour) along with FBZs of the 3C-phase structure (light blue contour) and the 2H-phase structure (blue contour). The X'' point is equivalent to the X point of the 3C structure and positioned at the edge of the new FBZ with coordinates (1/2, 0, 1/6) in fractions of reciprocal lattice vectors ($\mathbf{g}_1$, $\mathbf{g}_2$, $\mathbf{g}_3$′) of the 11-layer defect structure. $\mathbf{g}_1$ and $\mathbf{g}_3$′ are in-plane reciprocal lattice vectors as indicated by two arrows, while $\mathbf{g}_2$ is out-of-plane and not indicated here. The X'' point was further used to calculate the angle-resolved vibrational spectra. **d**, Integrated signal of the TA mode in the projected PDOS spectra in the energy range 30–40 meV.

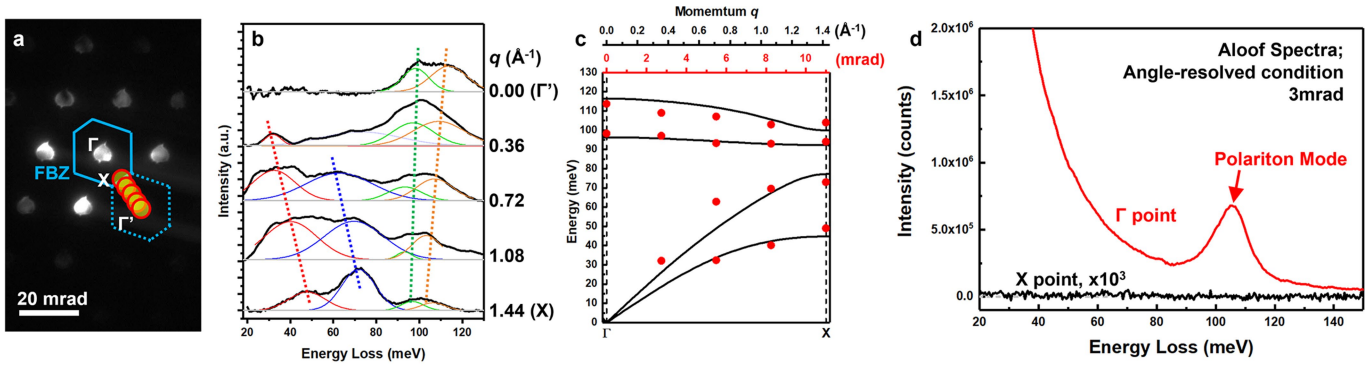


**Extended Data Fig. 6 | Angle-resolved vibrational spectra along X→Γ′ and phonon dispersions of all phonon branches in the defect-free SiC as well as aloof spectra of SiC film using a convergence semi-angle of 3 mrad.** **a**, Diffraction pattern of SiC with annotations including the FBZ (solid blue contour) and selected momentum positions of the EELS entrance aperture (red circles) along X→Γ′, where Γ′ is the centre of the adjacent BZ (dashed blue contour). **b**, Angle-resolved vibrational spectra along X→Γ′. The TA (red), LA (blue), TO (green) and LO (orange) modes are separated after multi-Gaussian peak fitting. Four dashed lines are guides to the eye to show the shift of corresponding modes at different momentum positions. The value of momentum $q$ is the reciprocal distance from the selected position to Γ′. **c**, Experimental phonon dispersion relation of the phonon energy (red points) from **b**, superimposed with the simulated phonon dispersion curves (black curves). In order to exclude the surface phonon polariton signal, the angle-resolved line-scan was acquired along X→Γ′ in the adjacent BZ rather than the FBZ. On the basis of the equivalence of each BZ, the angle-resolved phonon information along X→Γ′ should be identical to that along X→Γ. At the Γ′ point ($q = 0$ Å$^{-1}$), the LO and TO modes can be distinguished in the raw spectrum without the presence of the polariton signal, which is due to the long wavelength dipole scattering. TA and LA modes can also be detected at most momentum positions as shown in **b**, but were not easily separable at $q = 0.36$ Å$^{-1}$ because of their energy difference being smaller than the energy resolution. The experimental peak locations of all four branches are consistent with theoretical phonon dispersion curves as shown in **c**. The discrepancy between experiment and theory is much reduced compared to previous work[30], thanks to the improved energy resolution. **d**, Aloof spectra of SiC film with different momentum exchanges by angle-resolved vibrational spectroscopy. The convergence semi-angle was 3 mrad and spectra were obtained at the Γ point (centre of FBZ, red curve) and the X point (black curve) of the SiC film. Spectra were acquired when the electron beam was 20 nm from the surface of the SiC sample. The intensity of the X point spectrum is multiplied by 1,000. The polariton mode only appears in the aloof spectrum of the Γ point, which is consistent with the aloof spectrum acquired at large convergence semi-angle in main-text Fig. 2a.

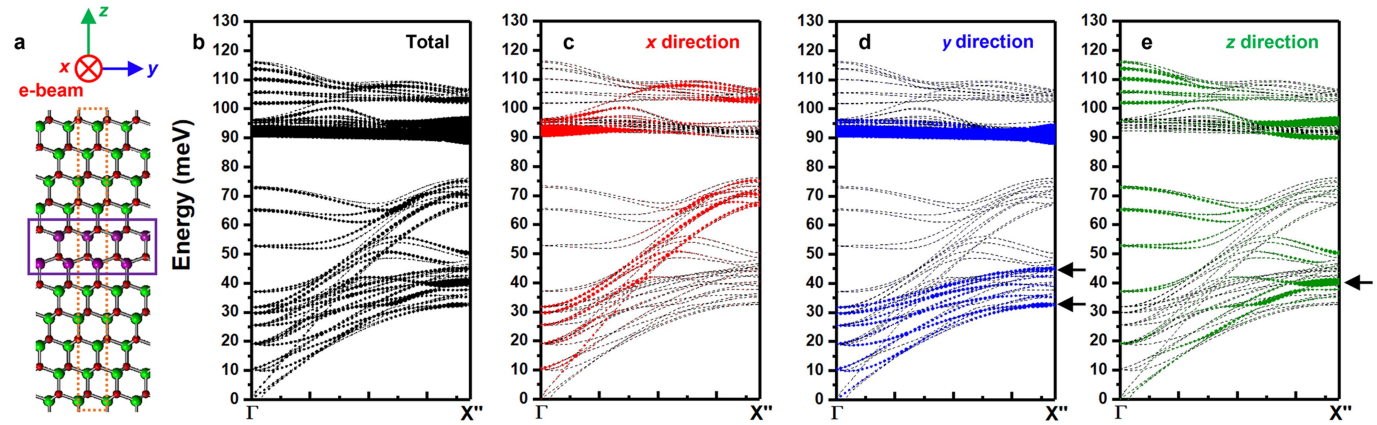


**Extended Data Fig. 7 | Contribution of local atomic vibrations at a stacking fault along three orthogonal directions. a**, Atomic structure of an 11-layer defect structure, showing **x**, **y** and **z** directions. The electron beam (e-beam) direction is parallel to the **x** direction in our experimental setup. **b**–**e**, Bubble plots of phonon dispersion of the structure shown in **a** along the Γ to X″ direction with the contribution of local atomic vibrations at the stacking fault (inside purple box) in all directions (**b**, black dots), and along **x** (**c**, red dots), **y** (**d**, blue dots) and **z** (**e**, green dots) directions. The X″ point is the same as shown in Extended Data Fig. 5c. The size of each dot (the 'bubble') represents the local vibrational density of states at the stacking-fault region. The density of states was calculated by summing the square of an eigenvector's amplitude for selected phonon modes and directions. In **b**–**e**, the calculated phonon dispersion curves are added as dashed curves. Vibrations along the electron beam direction (the **x** direction in **a** and **c**) cannot be detected in our experimental setup[44]. As a result, the vibrational spectrum at the stacking fault should comprise vibrations moving along both **y** and **z** directions in **d** and **e**.

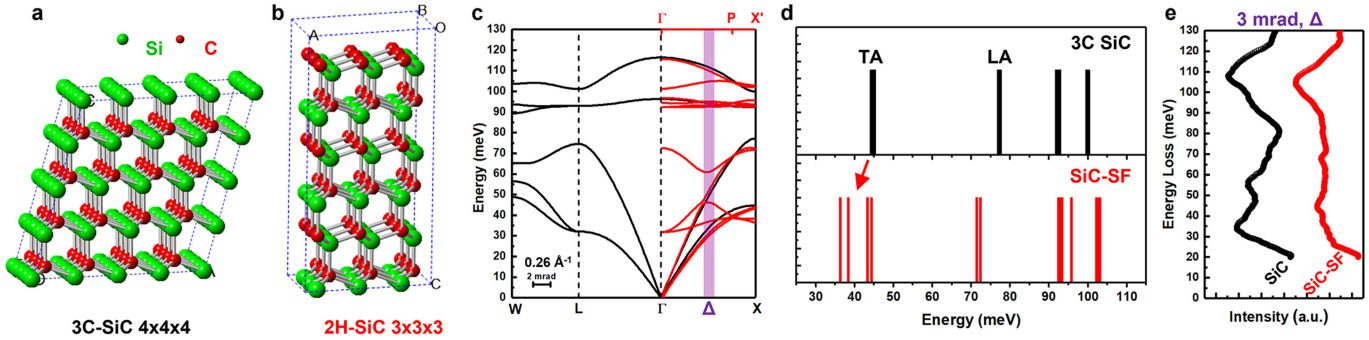


**Extended Data Fig. 8 | Atomic structure of simulated models and corresponding phonon dispersion curves. a**, 4 × 4 × 4 supercell of 3C SiC. **b**, 3 × 3 × 3 supercell of 2H SiC. **c**, Simulated phonon dispersion curves of 2H SiC (red) superimposed with those of 3C phase (black) in the Γ–X direction. The 2H phase was used to mimic the stacking-fault structure, and the Γ–P–X′ path in the 2H phase is identical to the Γ–X path in 3C phase, as mentioned in Extended Data Fig. 2. **d**, Energy positions of simulated phonon modes of the stacking fault (SiC-SF) and defect-free 3C-phase SiC in **c** at the X point. **e**, Vibrational spectra of defect-free SiC (black) and the stacking-fault region (red) with a convergence semi-angle of 3 mrad at the Δ point, which is the midpoint of the Γ–X line. The location of the Δ point is marked by a violet bar in **c**.

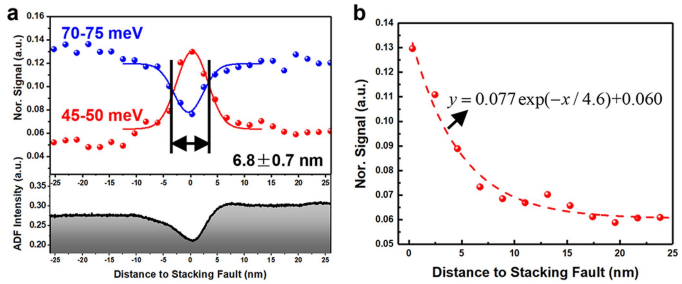


**Extended Data Fig. 9 | Spatial distribution of local phonon resonances.** **a**, Top panel, the TA (red dots) and LA (blue dots) signals were integrated in the respective energy ranges 45–50 meV and 70–75 meV using the spectrum image data in main-text Fig. 4b, and overlaid with Gaussian-type fitting curves. 'Nor.' means normalized with respect to the height of the ZLP in each spectrum. Bottom panel, ADF intensity of the STEM image in main-text Fig. 4a. **b**, Fitting of the signal intensity of TA as a function of the distance to the stacking fault. Red dots are duplicated from the positive $x$-axis data of the integrated intensity in the energy range 45–50 meV in **a**. The fitting function is indicated near the red dashed fitting curve, where $y$ is the signal intensity, and $x$ is the distance to the stacking fault. We estimated the decay length of the defect phonon mode near the stacking fault according to the one-dimensional Schrödinger equation for the quasiparticle (the defect phonon at the X point). The wavefunction ($\psi$) of the defect mode should decay exponentially outside the fault, following $\psi(x) = A\exp(-x/\xi)$, where $x$ is the distance away from the stacking fault and $A$ is a coefficient. The localization length, $\xi$, depends on the energy difference between the defect mode and corresponding TA mode in the defect-free region, $\Delta E_{\mathrm{Ph}}$ (3.8 meV in this case), and can be estimated from $1/\xi = \sqrt{2m^*\Delta E_{\mathrm{Ph}}}/\hbar$, where $m^*$ is the effective mass of the defect mode and $\hbar$ is the reduced Planck constant. Taking the effective mass from the phonon dispersion curve of 3C-phase SiC at the X point ($m^* \approx 2.03 \times 10^{-28}$ kg, only absolute values in the square root), $\xi$ is about 2.7 nm. This is close to the experimental observation, 4.6 nm, obtained through a fitting as shown in **b**. It appears that the relationship $1/\xi = \sqrt{2m^*\Delta E_{\mathrm{Ph}}}/\hbar$ holds well for estimating the decay length of local phonon modes.

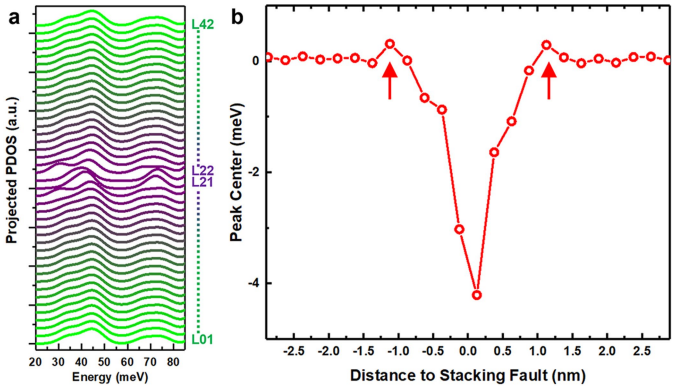


**Extended Data Fig. 10 | Local PDOS of the defect structure calculated by the real-space Green's function approach. a**, Projected PDOS plots corresponding to individual layers in a 42-layer structure at the X point. This structure was constructed by inserting a 2-layer stacking-fault structure into a periodic 3C-bulk SiC of 40 layers (each layer was designed as in Extended Data Fig. 5a, and the thickness of the 42-layer structure is about 10.5 nm). The stacking-fault structure was inserted at layers L21 and L22, marked on the right-hand side. Then, the retarded Green's function was calculated at the specific momentum, and simulation details followed the procedure in the literature[55]. The simulated results were broadened with a Gaussian peak of 8 meV FWHM, resulting in all curves as shown. **b**, Peak centre of the 40–50 meV TA mode as a function of distance to the stacking fault. This result predicted a 4-meV red shift of TA modes at 40–50 meV in **a**. Also, the variation extended to a distance of 1.125 nm around the stacking fault and affects a region 2.25 nm wide in total, which is much broader than the size of the stacking fault (0.25 nm). This broadening is closer to our experimental observation than the DFT results in Extended Data Fig. 5b.